FFEMS Fatigue & Fracture of Engineering Materials & Structures
SPECIAL ISSUE CONTRIBUTION
doi: 10.1111/ffe.12410

Crystal plasticity FE study of the effect of thermo-mechanical loading on fatigue crack nucleation in titanium alloys

D. OZTURK, A. SHAHBA and S. GHOSH

Department of Civil Engineering, Johns Hopkins University, Baltimore, MD , USA

Received Date: 29 October 2015; Accepted Date: 13 January 2016; Published Online: 19 February 2016

ABSTRACT In this paper, crystal plasticity simulations are conducted with a stabilized finite deformation finite element model to study the effects of microstructure as well as thermal and mechanical loading conditions on fatigue crack nucleation of Ti alloys. The crystal plasticity model includes a non-local crack nucleation model. Results of simulations are used to understand the effects of dwell loading periods and microtexture on fatigue nucleation life in polycrystalline microstructures in comparison with experiments. From the thermo-mechanical studies of these alloys, it is found that anisotropic thermal expansion under thermal loading can induce stresses normal to the basal plane, which can help opening up microcracks. Moreover, in agreement with experimental results, the simulations show diminished load shedding at elevated temperature because of weakening of plastic anisotropy.

Keywords crack nucleation; crystal plasticity model; dwell fatigue loading; load shedding; microtexture; thermal stress.

NOMENCLATURE

A_i	Surface area of grain i
A_{ij}	Common surface area between grains i and j
$\mathbf{B}, B$	Crack opening displacement vector and magnitude
b^α	Burgers vector
$\mathbf{B}_{CF}$	Closure failure of Burgers circuit
c	Equilibrium crack length
$\mathbf{C}, [C_{ij}]$	Fourth-order and Voigt representation of elasticity tensor
$\mathbf{E}^e$	Elastic Green–Lagrange strain tensor
$\mathbf{F}$	Total deformation gradient
$\mathbf{F}^e, \mathbf{F}^\theta, \mathbf{F}^p$	Elastic, thermal and inelastic components of deformation gradient
g^α	Slip system resistance
G^α	Shear modulus
K_c, K_{mix}, K_n, K_t	Critical, mixed, normal and shear intensity factors
m	Material rate sensitivity
MI	$< c >-$ axis misorientation index
$\mathbf{m}_0^\alpha$	Slip direction
N_{nucl}	Number of cycles to crack nucleation
n_{slip}	Total number of slip systems
$\mathbf{n}^b$	Normal to crack surface
$\mathbf{n}_0^\alpha$	Slip plane normal
Q^α	Activation energy
R	Crack nucleation parameter
$\mathbf{S}$	Second Piola–Kirchhoff stress tensor
$\boldsymbol{\alpha}$	Tensor containing thermal expansion coefficients
β	Ratio of shear to normal fracture toughness
$.\gamma^\alpha$	Plastic slip rate on slip system α
γ_s	Surface energy
θ	Temperature

Correspondence: S. Ghosh. E-mail: sghosh20@jhu.edu

$\boldsymbol{\Lambda}, \{\Lambda\}$ Tensorial and vectorial representation of Nye dislocation tensor
v Poisson's ratio
$\boldsymbol{\sigma}$ Cauchy stress tensor
$\rho^{\alpha}_{GF}, \rho^{\alpha}_{GP}$ Forest and parallel GND densities
$\rho^{\beta}_{GNDen}, \rho^{\beta}_{GNDs}, \rho^{\beta}_{GNDet}$ Vectorial components of GND
τ^{α} Resolved shear stress on slip system α
$\tau^{\alpha}_{GF}, \tau^{\alpha}_{GP}$ Short and long range impeding stresses because of GNDs
χ^{α} Back-stress
$\chi^{\alpha\beta}$ Slip system interaction matrix

INTRODUCTION

Titanium alloys with an *hcp* crystalline structure are used in components in automotive and aerospace industries because of their high strength to weight ratio, high fracture toughness and good corrosion resistance at elevated temperatures. Despite these attractive properties, these alloys suffer from time-dependent plastic deformation at temperatures lower than those at which diffusion-mediated processes occur. The accumulation of creep strain has been reported for applied stresses as low as 60% of macroscopic yield stress.[1] In addition to their sensitivity to room-temperature creep, Ti alloys are prone to early fatigue failure at cold temperatures. Experiments showed that dwell loading with finite hold times reduces the fatigue life compared with cyclic loading with no hold time.[2] It has also been observed that dwell debit, defined as the ratio of life under regular cyclic loading to that under dwell loading, increases with increasing applied macroscopic stress.

Sensitivity of dwell debit to dwell time and applied stress indicates that underlying time-dependent mechanisms contribute to the cyclic fatigue damage. Experimental evidence,[2–5] as well as micromechanical modelling efforts,[6–8] suggests that accumulation of creep strain at the grain level is a major time-dependent contributor to dwell fatigue. Dwell fatigue crack initiation sites are typically subsurface and characterized by faceted cracks within the α grains, indicating a quasi-brittle crack initiation of the grains. Electron backscattered diffraction imaging combined with quantitative tilt fractography method has revealed that facet surfaces lie within 5–10° off the crystallographic basal planes of primary α-grains.[9–12] These fractured α grains at the initiation sites tend to be oriented such that the crystallographic $\langle c \rangle$ − axis lies within 10–25° of the loading direction;[10,13] in other words, the basal plane is almost perpendicular to the loading direction, and are subjected to a large normal stress component under dwell loading.

On account of the *hcp* crystalline structure, α-Titanium alloys exhibit elastic and plastic anisotropy, with [0001] direction showing high resistance to plastic deformation and also higher elastic stiffness. The previously mentioned observations on relative orientation of the basal planes, facets and load direction suggest that the quasi-brittle fracture of the basal planes is driven by the large normal stresses incident on the basal planes of these *hard* grains. In addition, electron backscattered diffraction imaging has shown that these faceted α grains are typically surrounded by grains that are suitably oriented for plastic deformation, with a high Schmid factor (SF) for basal and/or prismatic slip.[9] This combination of neighbouring *soft* and *hard* grains has been hypothesized to trigger a time-dependent stress redistribution mechanism.[4,12] This load-shedding phenomenon, arising out of the elastic and plastic anisotropy of *hcp* crystals, is deemed to be a major cause of the premature crack initiation under dwell fatigue.

Grain-scale micromechanical modelling has also provided supporting evidence and insight on the mechanisms of heterogeneous grain-scale time-dependent creep in dwell fatigue. Rate-dependent crystal plasticity finite element (CPFE) models for Ti-6Al and Ti-6242 have been developed by Hasija *et al.*[6] and Deka *et al.*[7] to show the effect of time-dependent stress relaxation on the soft grains leading to stress concentration on the hard grain. Time-dependent creep occurs on the soft grain during each dwell cycle, while the response of the neighbouring hard grain has more of an elastic character. Because of the compatibility requirement, this local creep is accompanied by stress redistribution, resulting in a time-dependent stress concentration on the hard grain with large normal tensile components on the basal plane. This stress component progressively increases with dwell cycles. An experimentally validated rate-dependent and size-dependent CPFE model for Ti-6242 has been proposed by Venkatramani *et al.*,[14,15] where the effects of grain and colony size and also microstructural parameters such as SF, misorientation and fraction of the primary α phase on the load shedding behaviour were studied under creep and dwell fatigue loading. It has been shown that stress concentration on the hard grain increases with accumulating time-dependent plastic strain. The larger soft grain size and higher fraction of α phase have also been found to have detrimental effects, consistent with experimental observations.[3] The influence of the grain boundary morphology and relaxation time scales has been studied by Dunne *et al.*[8,16] using a rate-dependent crystal plasticity model, which incorporates geometrically necessary dislocations (GNDs) that provide a physical length scale for plasticity. It was also shown that

load-shedding on the hard grain is more pronounced under stress controlled rather than strain-controlled loading, suggesting the necessity for a stress-dependent criterion for dwell crack initiation. In a recent paper, Zhang *et al.*[17] have investigated the effect of temperature on the time scale associated with the load shedding during the dwell cycles. They argued that the rapid stress relaxation at elevated temperatures leads to the loss of load shedding behaviour above 200 °C. In this paper, it is argued that the reduction of plastic anisotropy of α-Titanium might be the underlying cause of the loss of dwell effect at temperatures above 200 °C.

Motivated by the observation that fatigue crack nucleation is considerably influenced by the crystallographic and morphological features of the microstructure, an experimentally validated microstructure-dependent crack nucleation model has been developed by Anahid *et al.*[18,19] to predict the microstructural location and cycles to crack nucleation for Ti alloys under dwell loading. The criterion is based on the development of stresses in the hard grain and the accumulation of dislocations in the soft grain near the grain boundary adjacent to the hard grain. Hierarchical models of deformation and crack nucleation have been initiated by Ghosh and Anahid,[20,21] taking into account the effects of the microstructural features such as grain size, crystallographic orientation, misorientation and microtexture.

In the present work, the crack nucleation model described in Refs. 18,19 is employed to study three important aspects controlling the dwell fatigue nucleation of Ti alloys. These include the following:

i investigation of the effect of mechanical loading profile, viz. dwell time on crack nucleation;
ii investigation of microstructure crystallographic features, e.g. grain-to-grain crystallographic misorientation on fatigue life; and
iii investigation of thermal loading on the fatigue life of components.

Two Ti alloys, viz. Ti-7Al (Ti-7) and Ti-6Al-2Sn-4Zr-2Mo (Ti-6242), are modelled in this paper under dwell fatigue loading. The predictive capability of the model is compared with established experimental observations. Parametric studies provide new insights into the role of thermo-mechanical environment on dwell fatigue crack nucleation. In the *Crystal Plasticity Finite Element Model* section, the crystal plasticity constitutive model along with some considerations for capturing thermal effects in the framework of CP is explained. This section concludes with an introduction to a stabilized locking-free crystal plasticity element formulation. The crack nucleation model is outlined in the *Microstructural Crack Nucleation Model* section. The predictive capability of this model is demonstrated in the *Numerical Results* section followed by concluding remarks in the *Summary and Conclusions* section.

CRYSTAL PLASTICITY FINITE ELEMENT MODEL

The alloy Ti-7 is a near-α alloy with an *hcp* crystalline structure, whereas Ti-6242 has a biphasic microstructure consisting of equiaxed primary α grains of *hcp* structure and transformed-β grains with alternating laths of α (*hcp*) and β (*bcc*) structures. The microstructure of Ti-6242 has been described in an earlier work .[7] This microstructure consists of 70% primary α grains and 30% transformed β grains. Within the transformed β grains, α and β laths are observed to have volume fractions of 88% and 12% respectively. To predict material response, it is important to represent relevant morphological and crystallographic features of the microstructure, such as grain size distribution, orientation distribution and misorientation distribution, in the 3D reconstructed virtual microstructures. The DREAM.3D software,[22] based on methods described in Refs. 23,24 has been used to reconstruct statistically equivalent 3D microstructures for both Ti-7 and Ti-6242 alloys as shown in Fig. 1. These microstructures are discretized linear constant strain tetrahedral (TET4) elements using Simmetrix® software.[25]

Plasticity in Ti alloys is primarily attributed to dislocation slip, where dislocations are inhomogeneously distributed into planar arrays because of short range ordering of Ti and Al atoms.[26] Twinning is another deformation mechanism contributing to plasticity in *hcp* metals, which is observed at low temperatures and high strain rate loading. Deformation twinning has been observed in unalloyed Ti at all temperatures below 500 °C.[27] However, alloying Ti with Al inhibits twinning such that titanium alloyed with %6 Al does not twin even at temperatures as low as 100 K.[28,29] These data show that twinning is not a major deformation mechanism for the problem of interest and need not be accounted for in the constitutive model. In this section, the experimentally validated size-dependent rate sensitive crystal plasticity constitutive model developed in Refs. 6,7,14,15,30 is briefly introduced. This is followed by a short discussion on temperature effects.

Crystal plasticity constitutive model

A crystal plasticity constitutive model for finite strain deformation of Ti alloys under general non-isothermal conditions is presented in this section. This model is non-local because of the incorporation of geometrically necessary dislocations (GNDs), which renders the model size-dependent. As illustrated in Fig. 2, the total deformation gradient $\mathbf{F}$ is multiplicatively decomposed of into elastic $\mathbf{F}^e$, thermal $\mathbf{F}^\theta$ and inelastic $\mathbf{F}^p$ components as

$$\mathbf{F} = \mathbf{F}^e\mathbf{F}^\theta\mathbf{F}^p \tag{1}$$

where $\mathbf{F}^e$ accounts for elastic stretching and rigid body rotations. $\mathbf{F}^\theta$ denotes the deformation of crystal lattice because of thermal changes and evolves as,[31]

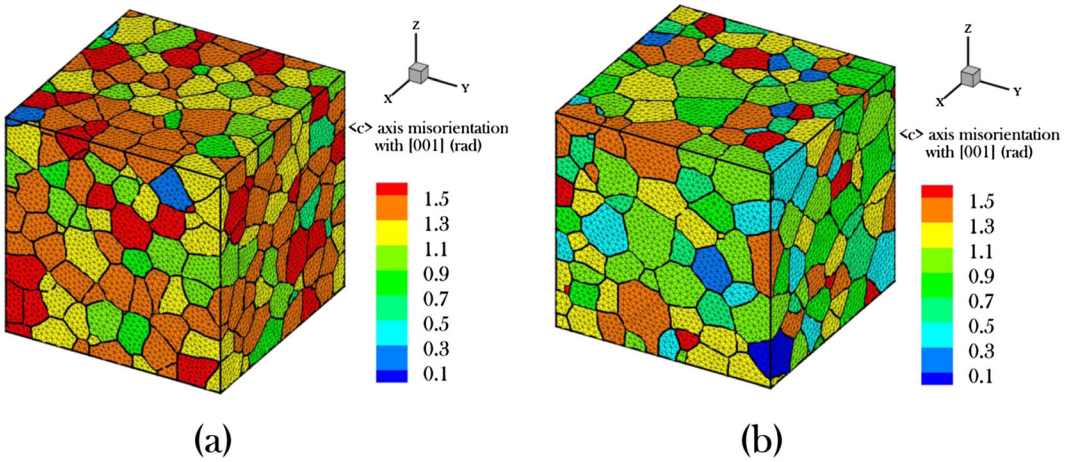

Fig. 1 Statistically equivalent 3D microstructures for (a) $680 \times 680 \times 680\,\mu m^3$ Ti-7 polycrystalline volume with 540 grains discretized into 583432 TET4 elements and (b) $29 \times 29 \times 29\,\mu m^3$ Ti-6242 polycrystalline volume with 503 grains discretized into 492733 TET4 elements.

$$\dot{\mathbf{F}}^{\theta} = \dot{\theta}\,\boldsymbol{\alpha}\mathbf{F}^{\theta} \tag{2}$$

where θ is the temperature and $\boldsymbol{\alpha}$ is a diagonal tensor with respect to principal crystallographic coordinate system containing thermal expansion coefficients along the principal crystallographic directions. $\mathbf{F}^p$ represents isochoric plastic deformation ($\det \mathbf{F}^p = 1$), where crystal lattice is neither distorted nor rotated. Using the kinematics of dislocation glide, the rate of evolution of $\mathbf{F}^p$ could be expressed in terms of slip rate $\dot{\gamma}^{\alpha}$ as[32]

$$\mathbf{L}^p = \dot{\mathbf{F}}^p \mathbf{F}^{p^{-1}} = \sum_{\alpha=1}^{n_{slip}} \dot{\gamma}^{\alpha} \mathbf{m}_0^{\alpha} \otimes \mathbf{n}_0^{\alpha} \tag{3}$$

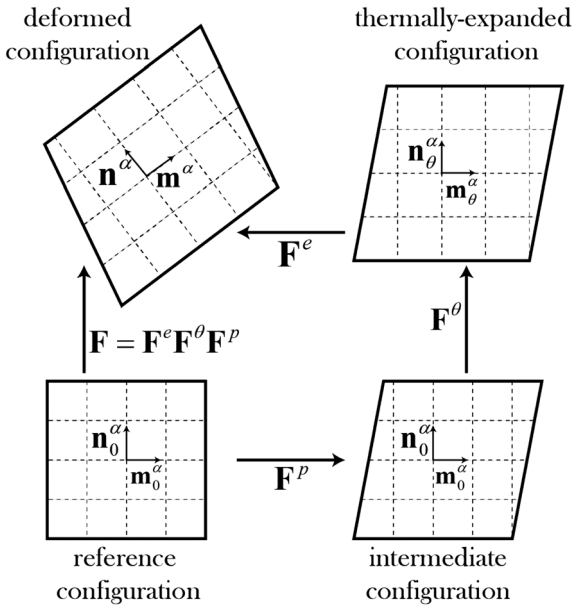

Fig. 2 Multiplicative decomposition of total deformation gradient $\mathbf{F}$ into elastic $\mathbf{F}^e$, thermal $\mathbf{F}^{\theta}$ and inelastic $\mathbf{F}^p$ components.

in which $\mathbf{L}^p$ is the plastic velocity gradient in the intermediate configuration, n_{slip} corresponds to number of slip systems and $\mathbf{m}_0^{\alpha}$ and $\mathbf{n}_0^{\alpha}$ are respectively slip direction and slip plane normal for slip system α in the reference configuration.

The constitutive equation in terms of second Piola–Kirchhoff stress $\mathbf{S}$ and elastic Green–Lagrange strain tensor $\mathbf{E}^e = \frac{1}{2}\left(\mathbf{F}^{e^T}\mathbf{F}^e - \mathbf{I}\right)$ in the thermally expanded configuration is expressed as

$$\mathbf{S} = \mathbf{C}(\theta) : \mathbf{E}^e. \tag{4}$$

$\mathbf{C}$ is the temperature-dependent fourth-order anisotropic elasticity tensor.

The plastic slip rate has a power law dependence on resolved shear stress τ^{α}, given as

$$\dot{\gamma}^{\alpha} = \dot{\tilde{\gamma}}^{\alpha} \left| \frac{\tau^{\alpha} - \chi^{\alpha} - \tau_{GP}^{\alpha}}{g^{\alpha} + \tau_{GF}^{\alpha}} \right|^{\frac{1}{m}} sign\left(\tau^{\alpha} - \chi^{\alpha} - \tau_{GP}^{\alpha}\right) \tag{5}$$

Here m and $\dot{\tilde{\gamma}}^{\alpha}$ are respectively the material rate sensitivity parameter and reference plastic shearing rate. χ^{α} is the back-stress, which accounts for kinematic hardening in cyclic deformation, and g^{α} is the slip system resistance because of evolution of statistically stored dislocations, which correspond to homogeneous plastic deformation. Effect of grain size on initial slip system resistance has been considered and incorporated through a Hall–Petch-type relationship.[14,15] Besides statistically stored dislocations, geometrically necessary dislocations (GNDs), which have a non-zero cumulative Burgers vector, are also present because of incompatibility of plastic strain near grain boundaries. GNDs contribute to the slip system resistances by providing short-range and long-range stresses,[33] given as

$$\tau^{\alpha}_{GF} = \frac{Q^{\alpha}}{c_2^{\alpha} b^{\alpha^2}} \sqrt{\rho^{\alpha}_{GF}} \ , \ \ \tau^{\alpha}_{GP} = {c_1}^{\alpha} G^{\alpha} b^{\alpha} \sqrt{\rho^{\alpha}_{GP}} \tag{6}$$

in which c_1^{α} and c_2^{α} are material constants and G^{α}, Q^{α} and b^{α} are respectively shear modulus, activation energy and Burgers vector for slip system α. ρ^{α}_{GP} and ρ^{α}_{GF} are respectively GND components parallel and normal to slip plane α, calculated as

$$\rho^{\alpha}_{GP} = \sum_{\beta=1}^{n_{slip}} \chi^{\alpha\beta} \left[\left| \rho^{\beta}_{GNDs} \sin\left(\mathbf{n}_0^{\alpha}, \mathbf{m}_0^{\beta}\right) \right| + \left| \rho^{\beta}_{GNDet} \sin\left(\mathbf{n}_0^{\alpha}, \mathbf{t}_0^{\beta}\right) \right| + \left| \rho^{\beta}_{GNDen} \sin\left(\mathbf{n}_0^{\alpha}, \mathbf{n}_0^{\beta}\right) \right| \right] \tag{7a}$$

$$\rho^{\alpha}_{GF} = \sum_{\beta=1}^{n_{slip}} \chi^{\alpha\beta} \left[\left| \rho^{\beta}_{GNDs} \cos\left(\mathbf{n}_0^{\alpha}, \mathbf{m}_0^{\beta}\right) \right| + \left| \rho^{\beta}_{GNDet} \cos\left(\mathbf{n}_0^{\alpha}, \mathbf{t}_0^{\beta}\right) \right| + \left| \rho^{\beta}_{GNDen} \cos\left(\mathbf{n}_0^{\alpha}, \mathbf{n}_0^{\beta}\right) \right| \right] \tag{7b}$$

where $\mathbf{t}_0^{\beta} = \mathbf{m}_0^{\beta} \times \mathbf{n}_0^{\alpha}$. ρ^{β}_{GNDs}, ρ^{β}_{GNDen} and ρ^{β}_{GNDet} are the vectorial components of GND density with Burgers vector parallel to $\mathbf{m}_0^{\beta}$. ρ^{β}_{GNDet} and ρ^{β}_{GNDen} are the edge components of GND density on slip system β with dislocation tangent line parallel to $\mathbf{n}_0^{\alpha}$ and $\mathbf{t}_0^{\beta}$, respectively. ρ^{β}_{GNDs} is the screw counterpart with dislocation tangent line parallel to $\mathbf{m}_0^{\beta}$. $\chi^{\alpha\beta}$ is the interaction matrix between slip systems α and β, taken as unity in this study. In order to calculate GND densities on different slip systems, it is necessary to evaluate Nye's dislocation tensor

$$\mathbf{\Lambda} = \sum_{\alpha=1}^{n_{slip}} b^{\alpha} \left(\rho^{\alpha}_{GNDs} \mathbf{m}_0^{\alpha} \otimes \mathbf{m}_0^{\alpha} + \rho^{\alpha}_{GNDen} \mathbf{m}_0^{\alpha} \otimes \mathbf{n}_0^{\alpha} + \rho^{\alpha}_{GNDet} \mathbf{m}_0^{\alpha} \otimes \mathbf{t}_0^{\alpha} \right) = \nabla^T \times \mathbf{F}^p \tag{8}$$

There are in general $3 \times n_{slip}$ unknown GND densities, which corresponds to 90 for *hcp* crystals. Of these, however, there exist only 63 independent densities including 9 ρ^{α}_{GNDs} s, 24 ρ^{α}_{GNDet} s and 30 ρ^{α}_{GNDen} s. Equation 8 could be rewritten as

$$\{\mathbf{\Lambda}\} = \mathbf{A}\{\rho_{GND}\} \tag{9}$$

where $\{\mathbf{\Lambda}\}$ is 9×1 vectorial representation of the Nye tensor, $\mathbf{A}$ is a 9×63 matrix containing the basis vectors and $\{\rho_{GND}\}$ is a 63×1 vector containing unknown GND densities. Equation 9 is an underdetermined system of equations. An L2 minimization approach has been proposed by Arsenlis and Parks[34] to solve Eq. 9 to obtain dislocation densities as

$$\{\rho_{GND}\} = \left(\mathbf{A}^T \mathbf{A}\right)^{-1} \mathbf{A}^T \{\mathbf{\Lambda}\} \tag{10}$$

Considering GNDs renders the constitutive model non-local and size-dependent. The material CP constants for each constituent phase and individual slip systems in this model have been experimentally calibrated and validated by Deka *et al.*[7] and Venkatramani *et al.*[14,30] against a large set of experiments including different constant strain-rate tests and creep tests under different load levels.

Temperature effects

Temperature changes play a critical role in mechanical behaviour of Ti alloys by affecting both elastic and plastic properties. In order to capture the effects of temperature changes in the framework of crystal plasticity, it is required to consider variation of both elasticity and plasticity-related constants with temperature. In Ti-6242, α titanium with an *hcp* lattice-parameter ratio $c/a = 1.59$ shows transverse isotropic elastic response, whereas β Ti shows cubic symmetry because of the *bcc* crystalline lattice. The anisotropic elasticity tensor in the Voigt notation may be written as

$$\left[C_{ij}\right] = \begin{bmatrix} C_{11} & C_{12} & C_{13} & 0 & 0 & 0 \\ & C_{22} & C_{23} & 0 & 0 & 0 \\ & & C_{33} & 0 & 0 & 0 \\ & & & C_{44} & 0 & 0 \\ & & & & C_{55} & 0 \\ sym. & & & & & C_{66} \end{bmatrix} \tag{11}$$

For α Ti, there are only five independent elastic constants, viz. $C_{11} = C_{22}$, C_{12}, $C_{13} = C_{23}$, C_{33}, $C_{55} = C_{66}$ and $C_{44} = (C_{11} - C_{12})/2$. In order to represent anisotropy for β Ti, only three independent elastic constants are required, viz. $C_{11} = C_{22} = C_{33}$, $C_{12} = C_{13} = C_{23}$ and $C_{44} = C_{55} = C_{66}$. Elastic constants for α and β phases have been calibrated at room temperature by Deka *et al.*[7] Experimental measurements for elastic constants of α Ti show that they decrease almost linearly with increasing the temperature, but with different slopes. The experimental results by Ogi *et al.*[35] are used to obtain the linear slopes for different elastic constants. Figure 3 depicts the variation of different principal elastic constants with temperature. The temperature dependence of Young's modulus for the simulated polycrystalline Ti-6242 model is also plotted in this figure, which also varies linearly with temperature. The linear slopes corresponding to the reduction of elastic constants with temperature

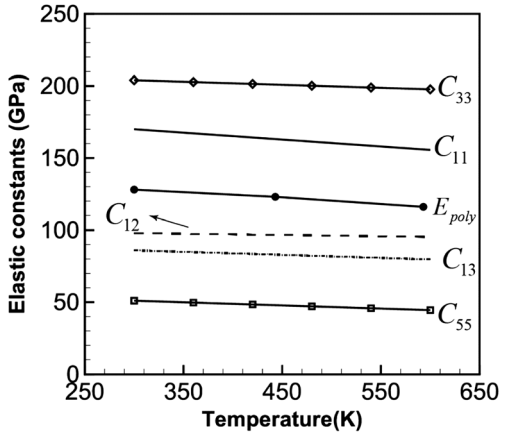

Fig. 3 Variations of elastic constants of α Ti, and the simulated Young's modulus of the polycrystalline Ti-6242 with temperature.

increase are given in Table 1. Because of lack of experimental results on variation of elastic constants for β-Ti in the temperature range of interest, the values of slopes are approximated by averaging the α-Ti slopes separately for the volumetric (C_{11}, C_{22}, C_{33}), normal-dilatational (C_{13}, C_{23}, C_{12}) and shear (C_{44}, C_{55}, C_{66}) elasticity coefficients, yielding respectively 39, 8.9 and 21.9 MPa K^{-1} for the β phase. The error introduced to the grain-scale variation of the stress fields, because of this uncertainty, is expected to be small, because the overall volume fraction of the β phase within the polycrystal is about 4%. The decrease in the Young's modulus of the simulated polycrystalline Ti-6242 model is 18 GPa over the temperature range of 300–650 K (E_{poly} shown in Fig. 3), which is in good agreement with the experimentally measured decrease (~20 GPa over 300–650 K) for polycrystalline Ti-6242 in the same (bi-modal) microstructural condition.[36]

Temperature changes also significantly influence the plastic behaviour because of thermally activated glide of dislocations. As temperature increases, the rate of successful thermal activation attempts is boosted up, and consequently, plastic flow is enhanced. In other words, the resistance to plastic flow reduces as temperature rises. In the crystal plasticity framework, each slip system has a slip resistance assigned to it. The experimental results reported by Williams *et al.*[29] for α Ti alloys are used here to derive the initial slip resistances for different *hcp* slip systems as a function temperature. The resistances

Table 1 Linear slopes for reduction of elastic constants of α Ti with temperature

Elastic constant	$C_{11}=C_{22}$	C_{12}	$C_{13}=C_{23}$	C_{33}	$C_{55}=C_{66}$
Linear slope $(^{MPa}/_{K})$	48	8.9	21	21	21.9

reported by Williams *et al.*[29] are shifted such that at room temperature they match the slip resistances reported in Deka *et al.*[7] Figure 4 shows the variation of slip resistances with temperature. The initial resistances are expressed in terms of temperature as

$$g^{\alpha}(\theta) = g_0^{\alpha} - \hat{g}^{\alpha}\left(1 - \exp\left(\frac{\theta - \theta_{ref}^{\alpha}}{\hat{\theta}^{\alpha}}\right)\right) \tag{12}$$

where g_0^{α} is the initial grain size-dependent slip system resistances calibrated at room temperature in Deka *et al.*[7] and $\hat{g}^{\alpha}$, θ_{ref}^{α} and $\hat{\theta}^{\alpha}$ are calibrated constants, given in Table 2. In this form, $\hat{g}^{\alpha}$ represents the part of the slip resistance that can be overcome with thermal activation. The test data of Williams *et al.*[29] for $\langle c+a \rangle$ slip show a transition to a steep softening response above 400 K. To represent this transition, a linear variation is assumed from room temperature up to 400 K given by $g^{\alpha}(\theta) = g_0^{\alpha} - (\theta - 300)\times 0.95$ MPa and an exponential decrease above 400 K given by $g^{\alpha}(\theta) = g^{\alpha}{}_{400\text{K}} - \hat{g}^{\alpha}\left(1 - \exp\left(\frac{\theta-\theta_{ref}^{\alpha}}{\hat{\theta}^{\alpha}}\right)\right)$ with $\theta_{ref}^{\alpha} = 400$ K. The difference in slip system resistances decrease as temperature increases. This implies that the material becomes more plastically isotropic with increasing temperature. Because of lack of experimental observation on temperature dependence of β-Ti slip system resistances in the literature, it is assumed that their dependence on temperature is similar to those of *hcp* basal systems.

Stabilization of constant strain tetrahedral elements for crystal plasticity finite element modelling

Modelling material behaviour and predicting localized phenomenon such as fatigue crack nucleation require accurate calculation of local material state variables like stresses and kinematic variables. This can only be achieved by using an appropriate material constitutive law and a robust computational framework that provides adequate resolution with accuracy. Given the requirement of mesh conformity to the computational domain, the complexity of polycrystalline microstructures often requires discretization of polycrystalline aggregates into tetrahedral elements. Linear constant strain tetrahedral elements (TET4) are preferred for CPFE simulations because of their capability in conforming to the complex geometries in the microstructure and inherent simplicity in the element formulation. However, these elements have been shown to suffer from volumetric locking resulting in spuriously increased stresses as the material approaches the incompressibility limit.[37,38] This locking induced instability can adversely affect the results of CPFE simulations in the presence of isochoric plastic deformation. The effect of volumetric

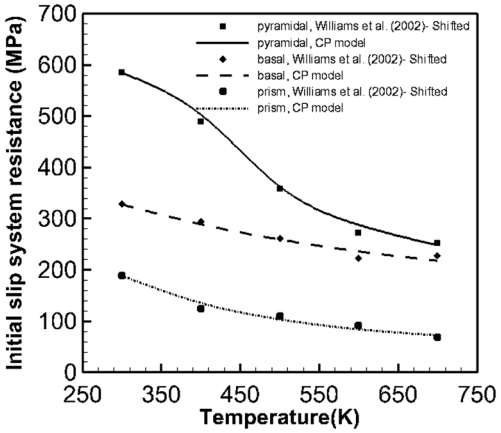

Fig. 4 Variation of initial slip system resistance with temperature for α-titanium.

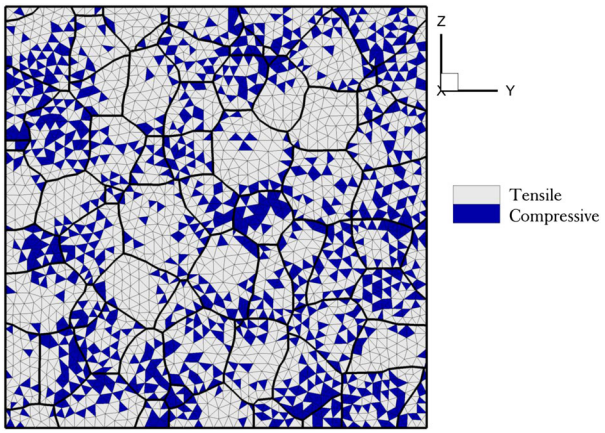

Fig. 5 Distribution of hydrostatic stress in the Ti-7 microstructure at 4.5% strain.

locking on local stress field in a CPFE simulation of polycrystalline Ti-7 alloy is shown in Fig. 5. The simulation is conducted for a constant strain-rate tensile test with $\dot{\varepsilon} = 9\times10^{-5}s^{-1}$ along the global z-axis. The instability in the form of spurious elemental hydrostatic stress on the YZ face of the microstructure after 500 s is shown in Fig. 5, depicting a checker-board distribution pattern.

A method of stabilizing TET4 elements and relieving volumetric locking for efficient and accurate CPFE simulations has been proposed in a recent paper by the authors.[39] In this model, the **F**-bar-patch method[40] has been incorporated into the CPFE framework. The **F**-bar patch method modifies the deformation gradient for stress tensor calculations, such that incompressibility is enforced over a patch of elements rather than on individual elements. This requires that elements in the mesh be assigned to non-overlapping patches. If P denotes a set of elements forming a patch, the modified deformation gradient for element $K \in P$ at time t is calculated as $\overline{\mathbf{F}}_K = \left[\frac{\Omega^t_{patch}}{\Omega^0_{patch}\det \mathbf{F}_K}\right]^{\frac{1}{3}} \mathbf{F}_K$ where $\mathbf{F}_K$ is deformation gradient of element K and Ω^t_{patch} and Ω^0_{patch} are respectively the current and undeformed volumes of the patch P. The modified deformation gradient $\overline{\mathbf{F}}_K$ is then used to solve constitutive law at the integration point of the element.

Table 2 Fitting constants for variation of slip system resistances with temperature

Calibrated constants	$\langle a\rangle$ – basal	$\langle a\rangle$ – prism	$\langle a\rangle$ – pyramidal	$\langle c+a\rangle$ – pyramidal (for $\theta > 400$K)
$\hat{g}^\alpha$ (MPa)	176.58	132.43	132.43	353
θ^α (K)	400	200	200	160
θ^α_{ref} (K)	300	300	300	400

MICROSTRUCTURAL CRACK NUCLEATION MODEL

Dislocation slip in *hcp* materials is highly orientation-dependent, as the critical resolved shear stress (CRSS) for hard slip mode, $\langle c+a\rangle$ – type slip on pyramidal planes, is approximately 3 – 6 times higher than the CRSS for easy slip modes, $\langle a\rangle$ – type slip on basal and prism planes.[41] During the hold period in dwell loading, grains which are properly oriented for $\langle a\rangle$ – type slip, undergo significant time-dependent plastic deformation, whereas the contiguous hard grains, which are less favourably oriented for $\langle a\rangle$ – type slip, experience large local stress concentrations near the shared grain boundaries from considerations of compatibility across the grain boundaries.[18,19] This phenomenon leads to stress re-distribution or load shedding that is considered to be responsible for early crack nucleation for dwell loading. Figure 6a and b show a soft grain 1 with a high basal SF and a moderate prism SF and a neighbouring hard grain 2 with low basal and prism SFs. As grain 1 is favourably oriented for dislocation slip on basal plane, it plastically deforms and causes load shedding on the neighbouring grain 2 as shown in Fig. 6c. The distribution of norm of Nye tensor, which is a measure for dislocation activity in the microstructure, is depicted in Fig. 6d. A higher value is observed in the soft grains close to neighbouring hard grain. Thus, the fatigue crack nucleation process in this case is dependent on both morphological and crystallographic features of the microstructure such as grain size distribution, grain orientation distribution, misorientation distribution and microtexture.

A microstructure-based crack nucleation model for polycrystalline Ti alloys under dwell fatigue loading has been proposed and experimentally validated by Anahid *et al.*[18,19] This model introduces crack nucleation in the hard grain because of plasticity in the adjacent soft grain. It encompasses the following characteristics:

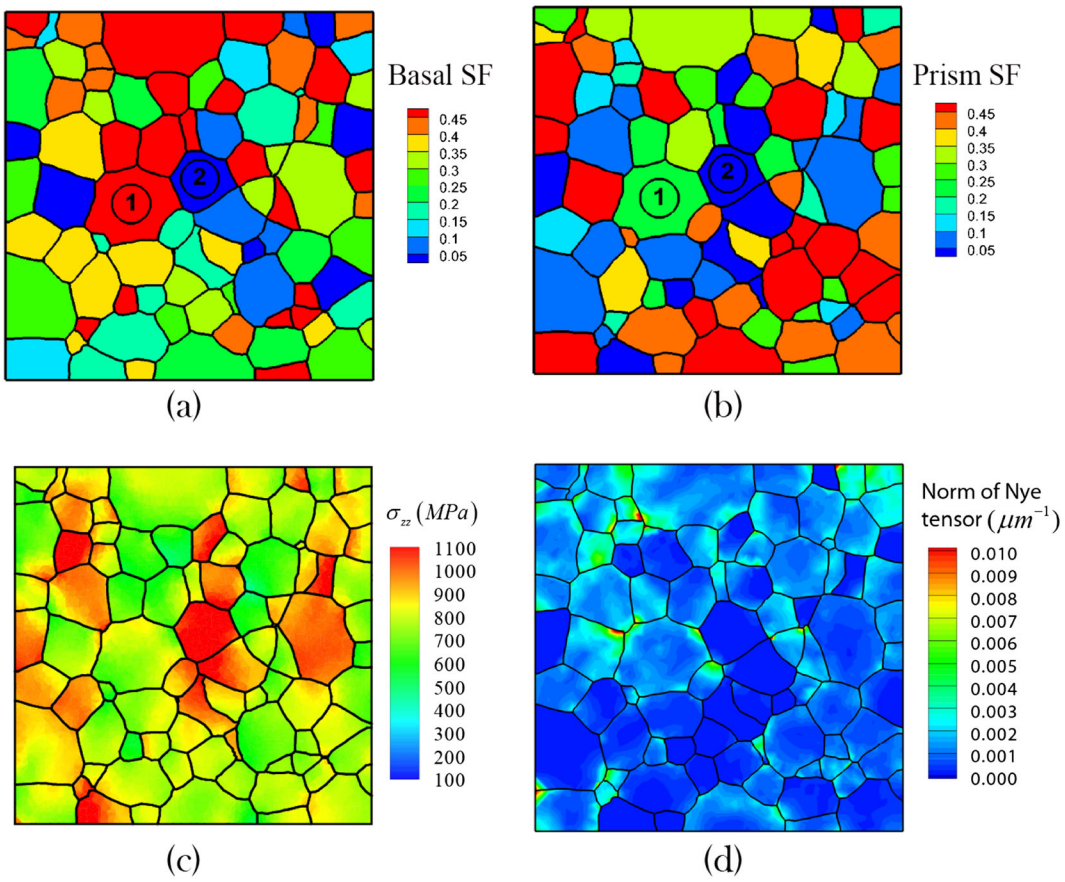

Fig. 6 Load shedding on hard grain 2 because of plasticity in adjacent soft grain 1 in polycrystalline Ti-6242 microstructure after 250 dwell cycles. Distribution of (a) basal Schmid factor, (b) prism Schmid factor, (c) σ_{zz} along the loading direction and (d) norm of the Nye tensor, indicating dislocation accumulation within the soft grains and at soft–hard grain boundaries.

i Wedge microcrack nucleates in the hard grain because of dislocation pileup in soft grain at the shared grain boundary.
ii Crack opening displacement corresponds to the closure failure along a Burgers circuit surrounding the piled-up dislocations.
iii Traction across the microcrack tip in hard grain opens up the crack.

The edge dislocation, defined as an extra half plane of atoms wedged between two perfect lattice planes, is equivalent to a microcrack with an opening displacement of one lattice constant. The opening displacement increases as deformation continues and more dislocations pile up at the grain boundary. In this section, this model is briefly introduced with some improvements.

Consider a soft-hard grain combination as illustrated in Fig. 7. The Nye dislocation tensor is used to measure the dislocation pile-up in the soft grain near the grain boundary. At point P, the closure failure of a Burgers circuit because of dislocations piercing an arbitrary plane with normal **n** in the soft grain could be calculated as

$$\mathbf{B}_{CF} = \int \mathbf{\Lambda} \cdot \mathbf{n}\, dA \tag{13}$$

For a grain discretized into elements, this integration is effectively calculated over the soft grain as

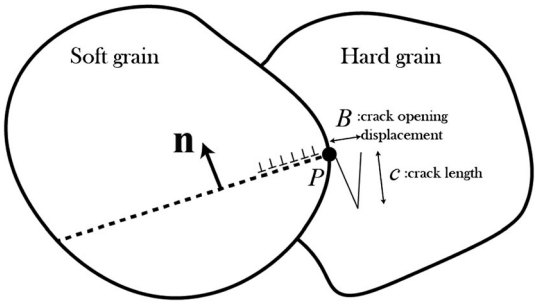

Fig. 7 Illustration of wedge-crack opening in the hard grain because of dislocation pile up in the adjacent soft grain.

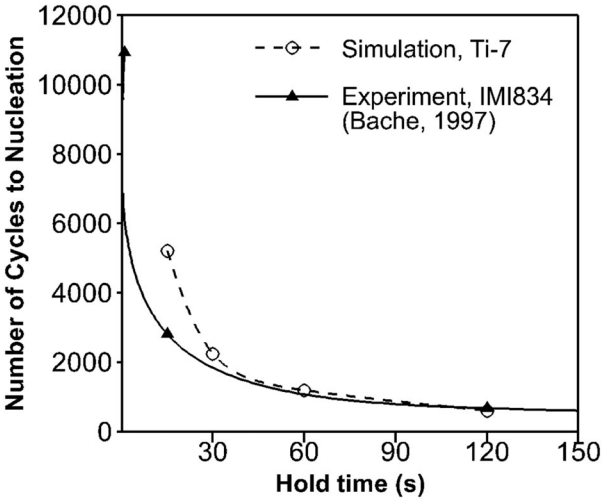

Fig. 8 Effect of dwell time on number of cycles to crack nucleation in Ti-7 polycrystalline model, compared with the experimental data for IMI834 reported by Bache (1997).

$$\mathbf{B}_{CF} = \sum_{e=1}^{N_e^{cut}} w_e A_e \mathbf{\Lambda}_e \cdot \mathbf{n} \tag{14}$$

Here N_e^{cut} is the number of elements in the grain, which are cut by a plane with normal $\mathbf{n}$ containing point P. A_e is the cross section area of the element cut by the plane and approximated as $A_e = \pi R_e^2$, in which R_e is the radius of a sphere which has the same volume as the element. $w_e = \exp\left(-r_e^2/4r_{\max}^2\right)$ is a weighting parameter signifying that the effects of dislocations on the crack opening displacement diminishes as the distance of the element centroid to point P, r_e, increases. $r_{\max}$ is distance of the furthest element centroid cut by the plane to point P.

Depending on the type of dislocations piercing the plane, the Burgers circuit closure failure can make any arbitrary angle with respect to the surface. For wedge-like cracks, the closure failure component lying in the surface, i.e. edge dislocation component, contributes to crack opening displacement. The crack opening displacement vector is hence calculated as

$$\mathbf{B} = \mathbf{B}_{CF} - (\mathbf{B}_{CF} \cdot \mathbf{n})\mathbf{n} \tag{15}$$

The crack opening displacement and crack surface normal are respectively given as

$$B = \|\mathbf{B}\| \quad , \quad \mathbf{n}^b = \frac{\mathbf{B}}{B} \tag{16}$$

The equilibrium length of crack may be calculated as $c = GB^2/8\pi(1-v)\gamma_s$ where v and γ_s correspond respectively to Poisson's ratio and surface energy.[42] The stress state in the hard grain helps the crack to open up. It is assumed[18,19] that cracks nucleate when the mixed-mode intensity factor $K_{mix} = \sqrt{K_n^2 + \beta K_t^2}$ is larger than a critical value K_c, i.e.

$$K_{mix} \geq K_c \tag{17}$$

β is the ratio of shear to normal fracture toughness and is set to 0.7071 in this study. Normal and shear intensity factors are respectively calculated as

$$K_n = \langle T_n \rangle \sqrt{\pi c} \quad , \quad K_t = T_t \sqrt{\pi c} \tag{18}$$

in which $T_n = \mathbf{n}^b \cdot (\boldsymbol{\sigma} \cdot \mathbf{n}^b)$ and T_t are respectively the normal and in-plane components of traction vector on the crack surface. The McCauley bracket is used for normal traction to signify that only tensile normal stress component aids the crack growth. The crack nucleation relation is derived from Eq. 17 as

$$R \geq R_c \text{ where } R = \sqrt{c\left(\langle T_n \rangle^2 + \beta T_t^2\right)} \text{ and } R_c = K_c/\sqrt{\pi} \tag{19}$$

This model is non-local in the sense that crack nucleates in the hard grain because of local stress field in the hard grain and the dislocation pile-up in the adjacent soft grain at the hard-soft boundary.

Implementation of the crack nucleation model

In order to determine the number of cycles to the first crack nucleation event N_{nucl}, every grain pair is examined in the post-processing stage of FE analysis. The maximum value R in the microstructure is obtained as follows:

i Each grain-pair in the microstructure is probed, and the two constituent grains are labelled as hard–soft grain pair based on the effective plastic strain.

ii The TET4 elements in the hard grain, which have a triangular face on the shared boundary, are determined. The nodes of these elements are the common nodes between the pair. The crack nucleation criterion in Eq. 19 is checked for these common nodes.

iii The highest stress intensity factor is calculated for each common node by the following steps.

a Sample the orientation space for $\mathbf{n}$ and determine the elements in the soft grain cut by a plane with normal $\mathbf{n}$.

b Using Eqs (14–16) calculate the normal to the crack surface $\mathbf{n}^b$ and crack opening displacement B. Normal and in-plane components of traction are then easily obtained.

c Stress intensity factor is calculated for every sample $\mathbf{n}$. The highest K_{mix} value corresponds to the critical $\mathbf{n}$ and $\mathbf{n}^b$.

iv As cracks nucleate over a finite area, the calculated nodal stress intensity factors at common nodes in the pair are

spatially regularized using a simple Gaussian function introduced for damage by Bažant and Pijaudier–Cabot.[43] This will lead to a much better convergence of stress intensity factor on mesh refinement.

Following the previously mentioned steps, the maximum value $R_{\max}$ in the entire microstructure is obtained. The cycles/time-to-crack nucleation corresponds to the time when $R_{\max}$ exceeds the critical value, R_c. Following steps delineated in the earlier study,[19] the critical value is obtained to be $R_c = 731.4\,\text{MPa}\sqrt{\mu\text{m}}$. This determination involves an improved method of calculating non-local closure failure in the Burgers circuit $\mathbf{B}_{CF}$ using the stabilized locking-free elements.

NUMERICAL RESULTS

Numerical examples are discussed in this section to study the effects of three aspects on crack nucleation of Ti alloys, viz. (i) dwell time in a dwell loading cycle, (ii) temperature in thermo-mechanical loading microtexture in polycrystalline aggregates and (iii) microtexture in polycrystalline aggregates. The dwell time analysis signifies the effects of loading profile on fatigue life, whereas the study on the effects of microtexture aims at understanding the importance of underlying microstructure on life. For dwell fatigue loading simulations, the tractions are applied along the global z-axis, and minimum displacement boundary conditions are applied to suppress rigid body translation and rotation. Each dwell loading cycle consists of 1 s of loading/unloading and 120 s of dwell hold, unless mentioned otherwise. The ratio of minimum to maximum applied traction in each cycle is 0.1.

Dependence of N_{nucl} on dwell time

To study the effect of dwell time on the number of cycles to crack nucleation, simulations are conducted for the Ti-7 polycrystals under different dwell loading cycles with hold periods of 15, 30, 60 and 120 s. Each loading cycle has a maximum applied traction of 572 MPa corresponding to ~95% of the macroscopic yield stress. The number of cycles to crack nucleation is plotted in Fig. 8 for different dwell periods. It is observed that N_{nucl} decreases dramatically as dwell time is increased because of the accumulation of time-dependent local strain during dwell periods and thus stronger load shedding mechanism. The simulated dependence of N_{nucl} on dwell time is in good agreement with the experimental data on IMI834 reported by Bache,[12] also shown in Fig. 8 for comparison. The results are also consistent with other experimental observations on the adverse effect of dwell period on fatigue life of Ti alloys, reported by Bache[2] and Sinha *et al.*[44] The ratio of N_{nucl} for 15 s of dwell period to the one for 120 s of dwell period is approximately 9. Results in Fig. 8 suggest that this ratio would even get larger with further reduction of dwell period, i.e. approaching perfect cyclic loading conditions. This is qualitatively in agreement with experimental results reported by Sinha *et al.*,[44] where dwell debit is reported to be 18 for applied stress of 95.5% yield stress.

Effect of temperature in thermal loading on crack nucleation

Titanium alloys are often exposed to both thermal and mechanical loading in their applications. In this section, the influence of temperature on load shedding and dwell crack nucleation is investigated to identify the thermo-mechanical conditions that adversely influence fatigue behaviour.

Loss of load shedding at elevated temperatures

Experimental observations have indicated the significance of dwell debit at temperatures below 200 °C.[2,12,44] However, it has been reported[44,45] that dwell debit diminishes at temperatures above 200 °C. The loss of dwell sensitivity at elevated temperatures has yet remained elusive. To study the micromechanical basis of this dwell sensitivity transition, several isothermal dwell fatigue loading simulations are conducted for the Ti-6242 alloy at temperatures ranging from 300 K (room temperature, 23 °C) up to 600 K (327 °C) in 100 K increments. As the yield stress drops with higher temperatures, the dwell load for each test temperature is set to 90% of the respective macroscopic yield stress for the sake of coherency in comparisons. The evolution of local stress component σ_{zz} after 1, 250 and 500 dwell load cycles is compared for ambient temperatures of 300 and 600 K in Fig. 9b and c. Local stresses are extracted along the line AB shown in Fig. 9a. Defining θ_c as the angle between the crystal $\langle c \rangle -$ axis and the loading direction, grains with $\cos(\theta_c)$ close to 1 correspond to the hard grains with negligible slip activity on basal and/or prismatic systems. Time-dependent concentration of stress in the hard grains, shown in Fig. 9, manifests that the load shedding mechanism is in effect at 300 K, while it clearly diminishes at 600 K.

To quantitatively evaluate the effect of the load shedding phenomenon at different temperatures, a *load shedding factor* is defined as the maximum local stress in a hard grain normalized by the applied external stress during the dwell period. Load shedding factors in the critical hard grain is plotted in Fig. 10 for different temperatures between 300 and 600 K. At and beyond 600 K, the level of time-dependent load shedding becomes insignificant because of the substantial decrease in plastic strength of

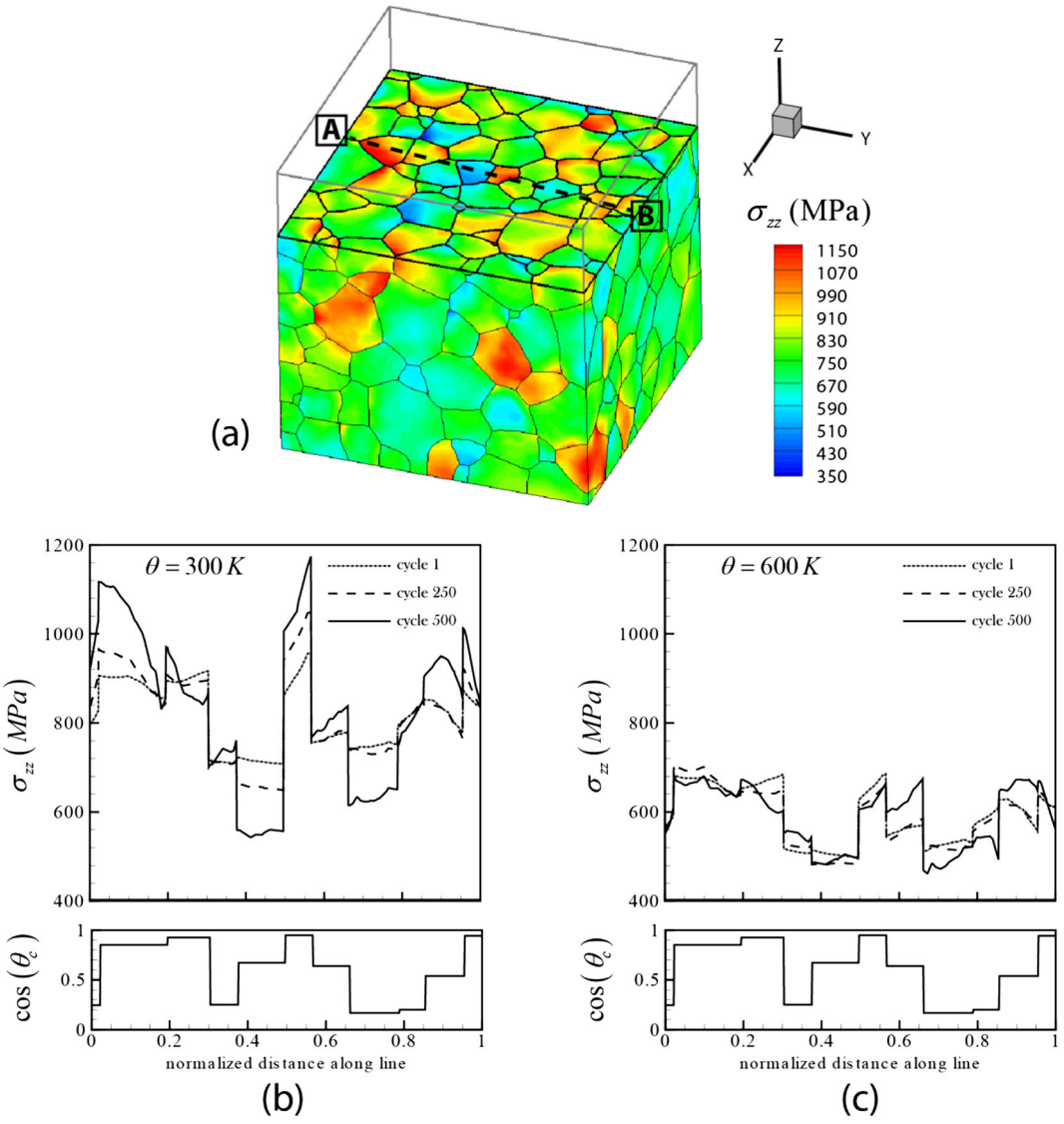

Fig. 9 Evolution of local stress σ_{zz} in Ti-6242 polycrystal under dwell fatigue loading at (b) 300 and (c) 600 K along the line AB shown in (a).

the *hcp* crystal along the [0001] direction (hard direction). In essence, plastic anisotropy of the *hcp* titanium, responsible for heterogeneous local creep and load shedding, is significantly reduced at elevated temperatures. This is evident from single crystal experiments conducted on Ti-Al alloys by Williams *et al.*,[29] as shown in Fig. 4. Slip resistances of the $\langle c+a \rangle$ – pyramidal slip systems are marked by a dramatic decrease above 400 K. The ratio of the CRSS for the $\langle c+a \rangle$ – slip systems to the one for $\langle a \rangle$ – basal system decreases from ~1.8 to ~1.2 from room temperature to 600 K. Results in the present simulations suggest that the diminution of load shedding as the time-dependent component of the fatigue damage accumulation might be responsible for the loss of dwell debit observed at elevated temperatures.

Effect of anisotropic thermal expansion on normal basal stresses

Several studies based on *ab initio* calculations and experimental observations have reported that *hcp* Ti crystals exhibit anisotropic thermal expansion over a wide range of temperatures.[46,47] In this work for Ti-6242, the thermal expansion coefficients for α phase along the principal crystallographic coordinate system are taken as $\alpha_{\langle a \rangle} = 1.8 \times 10^{-5}\,K^{-1}$ and $\alpha_{\langle c \rangle} = 1.1 \times 10^{-5}\,K^{-1}$.[47] The thermal expansion for β phase is isotropic with a thermal coefficient expansion of $\alpha = 0.9 \times 10^{-5}\,K^{-1}$.[48]

For a wide range of loading conditions, experimental observations suggest that both crack nucleation and short crack propagation in Ti alloys predominantly occur along

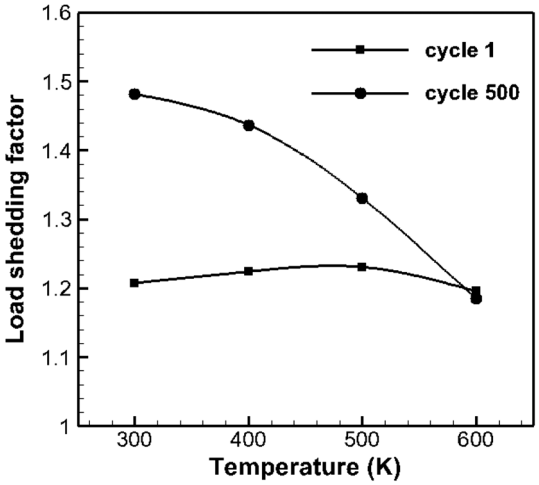

Fig. 10 Variation of load shedding concentration factor at different temperatures signifying the diminution of time-dependent load shedding at elevated temperatures in Ti-6242.

the basal plane.[11,49–51] Therefore, the stress component normal to the crystallographic basal plane is highly relevant to its fatigue response. Because the thermal expansion along [0001] direction is smaller than the in-plane basal expansion, the tensile normal stresses are induced on the basal plane under thermal loading. This may play an important role for crack nucleation and propagation in Ti alloys.

For an otherwise thermally isotropic material, which is free of external constraints, no thermo-elastic stresses would develop under a spatially uniform increase of temperature. However, because of the anisotropic thermal expansion of *hcp* titanium, a uniform increase of temperature within the polycrystalline aggregate induces thermal stresses because of the incompatibility of anisotropic thermal strains. To study the potential impact of grain-scale anisotropy-induced thermal stresses, thermo-elasto-plastic simulations are carried out for both Ti-7 and Ti-6242 alloys under a thermal loading profile. The load profile is made to approximately correspond to flight conditions for an aircraft. The thermal cycle has a spatially uniform increase of temperature from 300 to 750 K over 10 min, followed by a 1 h temperature hold at 750 K and eventually a 10 min long cool-down to room temperature. The minimum boundary conditions are applied to the polycrystalline model to suppress rigid body motions. Figure 11 shows the tensile normal traction developed on the basal planes after 50 min on representative cross sections. Only tensile tractions are of interest in this paper as they may facilitate mode I crack opening on basal planes. For both Ti-7 and Ti-6242 microstructures, the maximum local values of tensile normal stress on basal planes are observed to be as high as 700 MPa for this temperature increase of 450 K. Resolved shear stresses for basal and prismatic slip are negligibly small and do not induce considerable microplasticity. The stress concentrations typically occurred at the grain boundaries with high misorientation. Grain-averaged normal basal stresses are as high as 350 MPa, and they vary with the degree of misorientation of each individual grain with its neighbours. The range and distribution of the magnitudes of tensile normal stresses on the basal planes are very similar for both materials, suggesting that both α and near-α classes of Ti alloys may be affected by this mechanism, as long as the thermal expansion anisotropy of the α-phase is significant.

A parametric study is conducted to quantify the effects of $< c >$ – axis misorientation of neighbouring grains, on the basal normal stresses developed under thermal loading. The two-grain system illustrated in Fig. 12a is

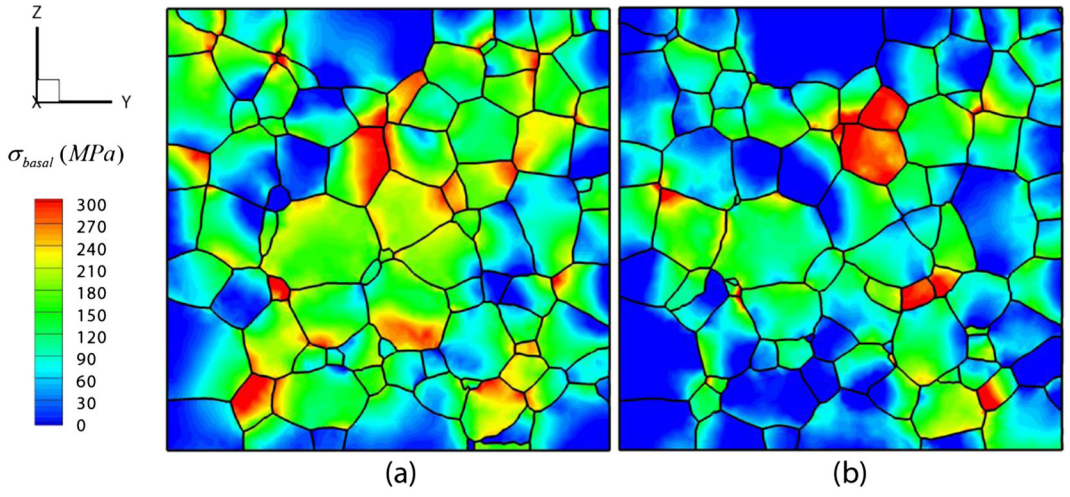

Fig. 11 Tensile normal tractions developed on basal planes in (a) Ti-7 and (b) Ti-6242 polycrystals, because of the anisotropic thermal expansion of hcp Ti.

modelled for a 200 s period, over which the temperature linearly rises from 300 to 750 K. The $< c >-$ axis of the inner grain is rotated with respect to the outer grain to generate a range of misorientations. A $< c >-$ axis misorientation index of grain a with its neighbouring grains is defined as $MI = 1 - \sum_b \frac{A_{ab}}{A_a} |\mathbf{c}_a \cdot \mathbf{c}_b|$, where $\mathbf{c}_a$ and A_a respectively denote $< c >-$ axis and surface area of grain a and A_{ab} is the common surface area between grains a and b. The summation is performed over all grains neighbouring grain a. It is evident that MI is zero if the $< c >-$ axes of the two neighbouring grains are aligned parallel to each other. The maximum and grain-averaged normal basal stresses induced in the inner grain as a function of MI are plotted in Fig. 12b. It is observed that the system will not experience any stress if $< c >-$ axes of the two grains are parallel to one another. However as MI increases, higher tensile stresses develop on the basal plane of the inner grain, which can potentially assist crack opening on these planes.

To evaluate the effect of the crystallographic texture on normal basal stresses within a polycrystalline sample, the response for a strong basal texture, typically seen in rolled titanium, is compared with the reference case of the Ti-6242 sample whose texture is based on a forged Ti-6242 specimen.[7] The rolled basal texture is synthetically generated, and its pole figure is shown in Fig. 13a, in addition to that of the forged Ti-6242. The same polycrystalline grain structure is used for both textures. The grain-averaged normal basal stresses after 50 min during thermal hold are plotted in Fig. 13b for the two textures. It is seen that grains with high MI experience higher basal tensile stresses. Because the misorientation is less on the rolled texture, anisotropy-induced thermal stresses are smaller. These results suggest that rolled Ti alloys will experience lower thermal stresses in comparison with the forged one in environments prone to temperature changes.

Influence of microtexture on dwell crack initiation

Many studies have been conducted for understanding the dependence of fatigue life on microstructural properties such as the grain-size, microtexture and macrotexture, α-grain volume fraction, lamellae-size and prior-β grain size in multiphase near α and $\alpha+\beta$ alloys.[11,52] This section is aimed at illuminating the effects of microtexture on microplasticity, load shedding, dwell crack nucleation and fatigue life. The α grains that nucleate from the same prior β grain during cool-down obtain similar crystallographic orientations and form microtextured regions. The size and extent of these microtextured regions are effectively controlled by the size of the prior β grains and the thermo-mechanical processing above the β-transus temperature. It is documented in the literature that large microtextured regions, favourably oriented for easy basal or prismatic plastic slip, lead to early dwell fatigue failure.[9,45,49] Representing microtextured regions as a single soft grain , it was shown by Venktaramani *et al.*[14] that the amount of stress concentration because of load shedding increases with the size of the soft region.

To study the effect of microtexture on dwell fatigue response, two polycrystalline models with the same morphology and orientations but different levels of microtexture are studied. The overall texture corresponding to the forged Ti-6242 microstructure, shown in Fig. 1b, is adopted as starting data. Using an iterative algorithm the grain orientations are swapped between grain pairs to generate two misorientation distributions

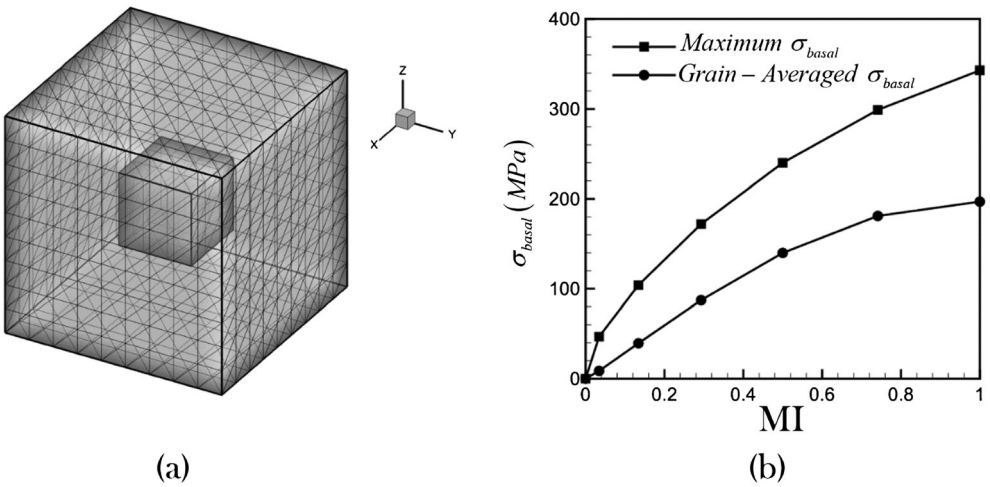

Fig. 12 (a) Two-grain model discretized into 4374 TET4 elements, (b) effect of $< c >-$ axis misorientation on normal basal stresses induced in the inner grain because of anisotropic thermal expansion.

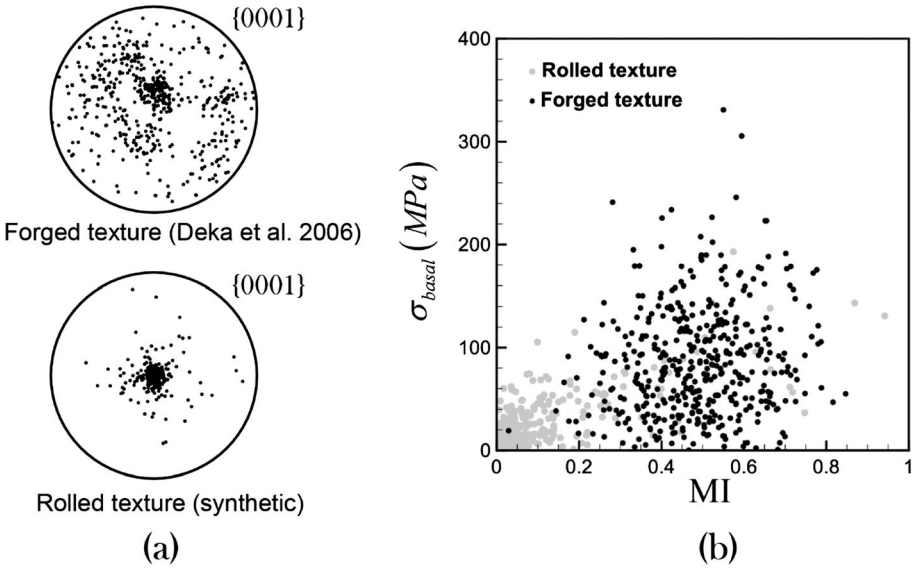

Fig. 13 (a) {0001} pole figures for rolled and forged textures assigned to the Ti-6242 polycrystalline model, (b) distributions of grain-averaged normal basal stresses versus the grain $< c >$ – axis misorientation index, for the two textures.

with low and high average misorientations. These two limiting cases of misorientation distribution, referred to as MS^{tex} and MS^{mis}, are shown in Fig. 14a. MS^{tex} corresponds to a microstructure, in which grains with similar orientations are clustered together to form microtextured regions. On the other hand, MS^{mis} corresponds to a microstructure, in which grains with disparate orientations tend to neighbour each other, resulting in a microstructure devoid of microtexture. These two microstructures are depicted in Fig. 14b.

Dwell fatigue simulations are conducted under 750 MPa corresponding to 90% macroscopic yield stress of the microstructure shown in Fig. 1b. Investigation of both microtextured and highly misoriented microstructures reveals significant differences in their microplastic responses. Figure 15 shows the distribution of the local stress component σ_{zz} and the local plastic strain after 500 dwell cycles at representative cross sections in both microstructures, along with the predicted location of the crack nucleation and crack plane in MS^{tex}. The response of MS^{tex} is characterized by (i) significant plastic strain accumulation within the clusters of similarly oriented grains that are favourably oriented for plastic slip, (ii) confinement of plastic deformation to these microtextured regions and ending abruptly at the boundaries adjacent to hard grain clusters, and (iii) stress concentration because of load shedding occurring predominantly at boundaries of the hard microtextured regions. These features result in a dwell

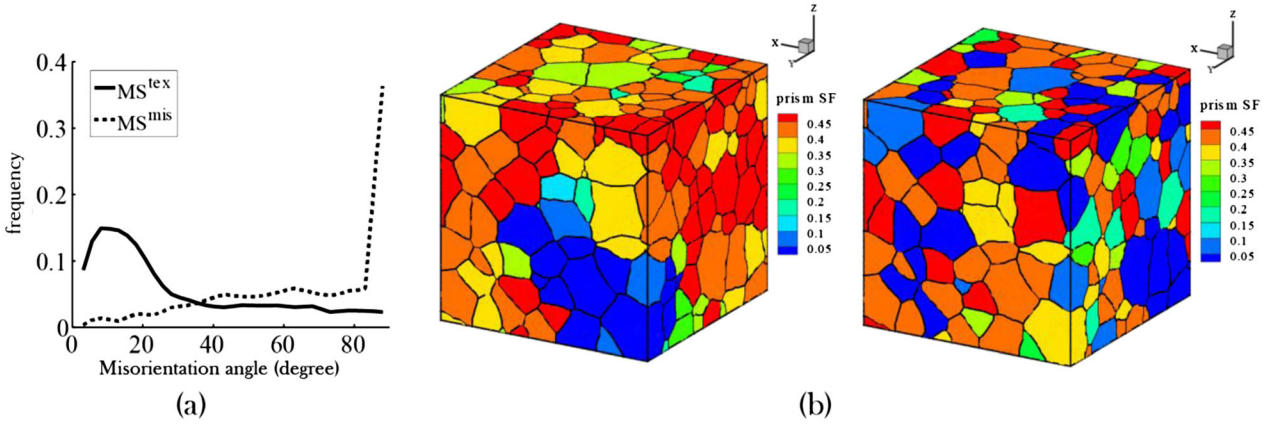

Fig. 14 (a) The two limiting cases of misorientation distributions applied to the Ti-6242, MS^{tex} (microtextured) and MS^{mis} (high-misorientation), (b) plots of the prismatic Schmid factors, visualizing the resulting clustering of the grain orientations as microtextured regions in MS^{tex} (left), in comparison to MS^{mis} (right).

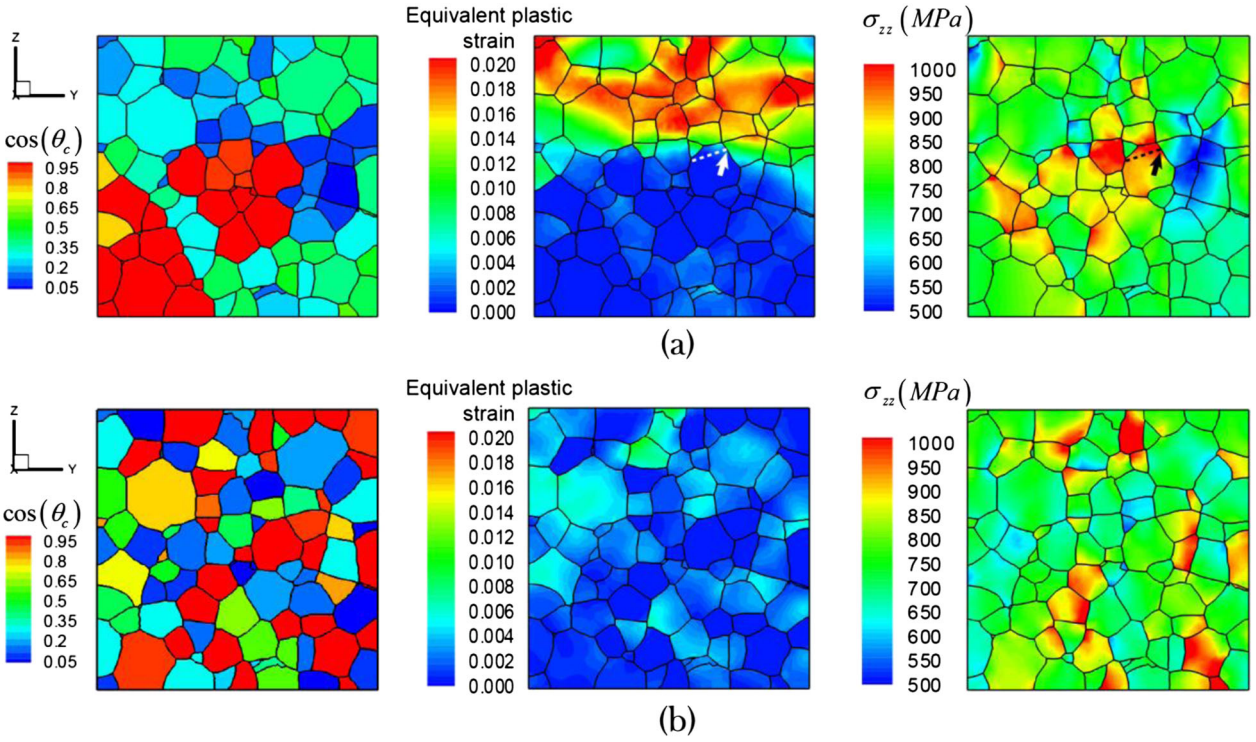

Fig. 15 Distribution of cos(θ_c), plastic strain and local stress σ_{zz} after 500 dwell cycles for (a) MS^{tex} (microtextured) and (b) MS^{mis} (high-misorientation) models of Ti-6242. Predicted location of crack initiation (arrow) and the trace of the crack plane (dashed line) are shown in (a).

crack nucleation at the boundary of a hard microtextured region, neighbouring a soft region as shown in Fig. 15a. The highly misoriented microstructure MS^{mis} exhibits milder and less variable response of local plasticity and stress compared with the response of MS^{tex}. The lack of clustered soft grains and grain-scale alternation of plastic anisotropy results in a fibre -like strengthening effect, suppressing plastic strain accumulation in the grains as shown in Fig. 16. Consequently, load shedding is less pronounced in this microstructure. These results are consistent with the experimental observations that microtextured regions facilitate plastic strain accumulation.[11] Such a difference in microplasticity between these two microstructures is interesting given that both MS^{mis} and MS^{tex} have the same grain morphology and texture.

The evolution of the crack nucleation parameter R for MS^{tex} and MS^{mis} is plotted in Fig. 17 along with the pole figures of the forged Ti-6242 texture. The dwell crack nucleation model predicts an earlier crack nucleation for MS^{tex}. The hard grain predicted by the model as the initiation site for dwell fatigue crack is located at a microtextured region with low basal and prismatic SF, adjacent to a cluster of soft grains with high prismatic SF.

A new set of orientations are generated synthetically, as shown in Fig. 18a, to verify these results and confirm that the predicted effects of microtexture persist over different textures. The grain orientations are then reassigned using the aforementioned iterative algorithm to obtain the two limiting cases. The same observations are made on the distribution of microplasticity and stress concentrations, and the microtextured model was observed to be more critical in terms of crack nucleation as shown in Fig. 18b.

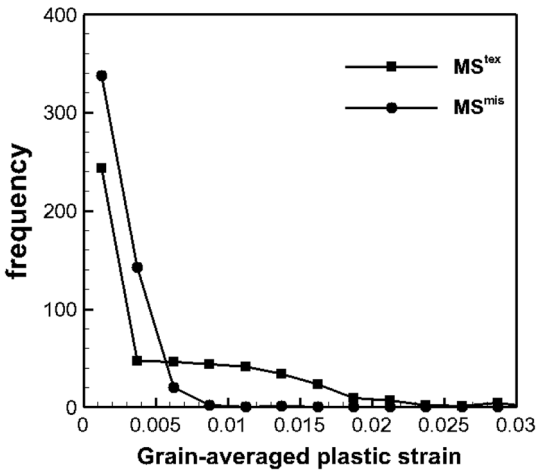

Fig. 16 Distribution of grain-averaged plastic strain after 500 dwell cycles for MS^{tex} and MS^{mis} models of Ti-6242, showing the incidence of grains with large plastic strain accumulation, and high variability in plastic strain within MS^{tex}, in contrast to a lower and more uniform plastic strain distribution in MS^{mis}.

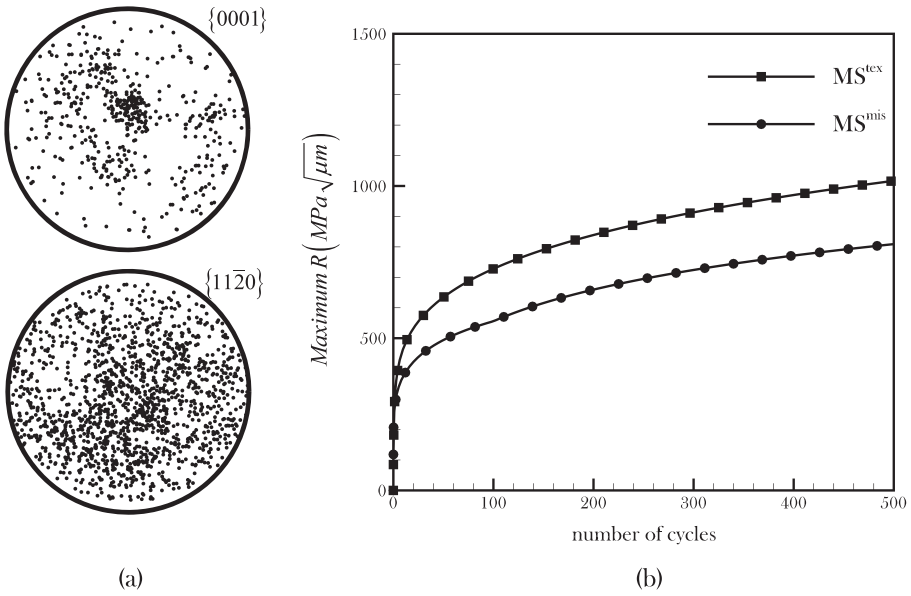

Fig. 17 (a) Pole figures for forged Ti-6242 texture and (b) evolution of maximum R for MS^{tex} and MS^{mis} models.

SUMMARY AND CONCLUSIONS

This paper develops a stabilized CPFE model, incorporating a rate sensitive size-dependent crystal plasticity constitutive law, to perform thermo-mechanical simulations for studying crack nucleation in polycrystalline Ti alloys. The simulations are used to comprehend factors that are responsible dwell fatigue crack nucleation in polycrystalline microstructures of these alloys. A crack nucleation model that has been developed by Anahid *et al.*[18,19] is employed to predict crack nucleation in the polycrystalline microstructures.

Three important aspects regarding dwell fatigue crack nucleation are studied. These are respectively the cyclic load profile, temperature in thermo-mechanical loading and local microstructural features. For the study on the cyclic loading profile, the effect of hold or dwell time on the number of cycles to crack nucleation is studied. The model predicts that as dwell time reduces and fatigue loading approaches a regular cyclic loading profile, the

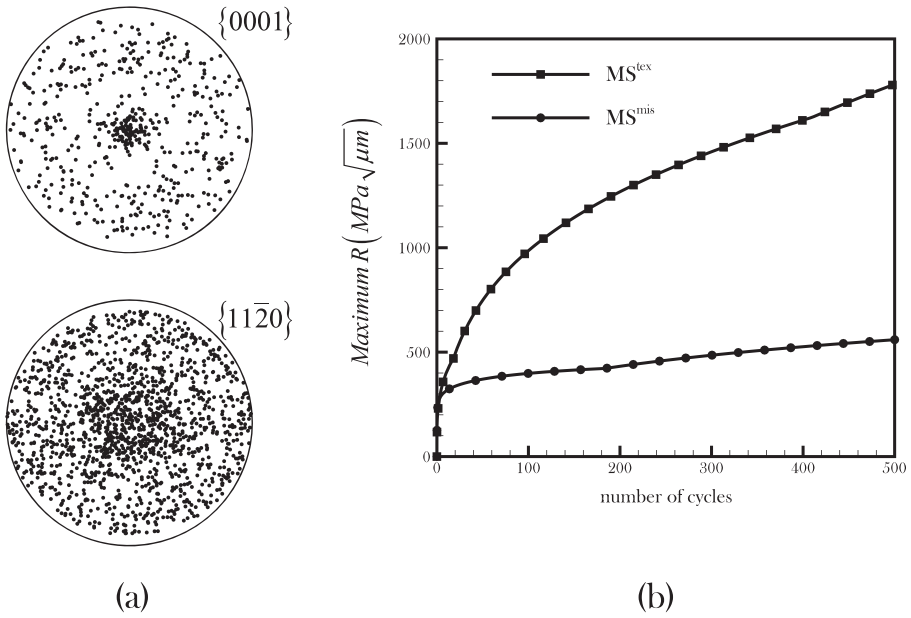

Fig. 18 (a) Pole figures of the synthetically generated texture for Ti-6242 and (b) evolution of maximum R for MS^{tex} and MS^{mis} models.

number of cycles to the first crack nucleation event increases. This is in agreement with experimental observations and signifies the adverse effects of dwell fatigue loading on the life of components. In the second study, the effect of temperature and thermo-mechanical loading on stress redistribution is studied, in light of the anisotropic thermal properties of Ti alloys. It is shown that thermal loading can induce tensile stresses on basal planes even under free expansion conditions because of the anisotropy of thermal expansion coefficients. These thermally induced stresses are larger for grains with high misorientation with respect to their neighbours. Orientation-sensitive basal normal stresses can facilitate crack nucleation and early crack propagation in Ti alloys and are important variables in a fatigue analysis. Moreover, the CPFE simulation results are able to reproduce the experimentally observed diminution of dwell effects at elevated temperatures. Within the framework of this model, this phenomenon is explained by the weakening of plastic anisotropy and correspondingly, suppression of time-dependent load shedding mechanism. To highlight the effects of microstructure on the life of Ti alloys under dwell fatigue loading, the influence of microtexture is investigated by simulating two models with high and low levels of microtexture. In agreement with experiments,[9,45,49] the simulations predict that the microtextured regions are more critical in dwell fatigue. This is because of higher rate of accumulation of plastic strains and a stronger load shedding mechanism.

Acknowledgements

This work has been supported through a subcontract to JHU (subrecipient) from the Ohio State University (main recipient) through a subaward No. 60038238 from an AFRL grant No. FA8650-13-2-2347 as a part of the AFRL Collaborative Center of Structural Sciences. The program managers of this grant are Dr. R. Penmetsa and Dr. R. Chona, and the PI is Prof. J. McNamara. This support to JHU is gratefully acknowledged. It has also been partially supported by the Army Research Office through grant no. W911NF-12-1-0376 (Programme Manager: Dr. A. Rubinstein). Computer use of the Hopkins High Performance Computing facilities is gratefully acknowledged.

REFERENCES

1 Odegard, B. C. and Thompson, A. W. (1974) Low temperature creep of Ti-6 Al-4 V. *Metall. Trans.*, **5**, 1207–1213.
2 Bache, M. (2003) A review of dwell sensitive fatigue in titanium alloys: the role of microstructure, texture and operating conditions. *Int. J. Fatigue*, **25**, 1079–1087.
3 Kassner, M. E., Kosaka, Y. and Hall, J. S. (1999) Low-cycle dwell-time fatigue in Ti-6242. *Metall. Mater. Trans. A*, **30**, 2383–2389.
4 Evans, W. J. and Bache, M. (1994) Dwell-sensitive fatigue under biaxial loads in the near-alpha titanium alloy IMI685. *Int. J. Fatigue*, **16**, 443–452.
5 Sinha, V., Mills, M. J. and Williams, J. C. (2006) Crystallography of fracture facets in a near-alpha titanium alloy. *Metall. Mater. Trans. A*, **37**, 2015–2026.
6 Hasija, V., Ghosh, S., Mills, M. J. and Joseph, D. S. (2003) Deformation and creep modeling in polycrystalline Ti–6Al alloys. *Acta Mater.*, **51**, 4533–4549.
7 Deka, D., Joseph, D. S., Ghosh, S. and Mills, M. J. (2006) Crystal plasticity modeling of deformation and creep in polycrystalline Ti-6242. *Metall. Mater. Trans. A*, **37**, 1371–1388.
8 Dunne, F. P. E., Rugg, D. and Walker, A. (2007) Lengthscale-dependent, elastically anisotropic, physically-based hcp crystal plasticity: application to cold-dwell fatigue in Ti alloys. *Int. J. Plast.*, **23**, 1061–1083.
9 Sinha, V., Spowart, J. E., Mills, M. J. and Williams, J. C. (2006) Observations on the faceted initiation site in the dwell-fatigue tested ti-6242 alloy: crystallographic orientation and size effects. *Metall. Mater. Trans. A*, **37**, 1507–1518.
10 Sinha, V., Mills, M. J. and Williams, J. C. (2007) Determination of crystallographic orientation of dwell-fatigue fracture facets in Ti-6242 alloy. *J. Mater. Sci.*, **42**, 8334–8341.
11 Szczepanski, C. J., Jha, S. K., Larsen, J. M. and Jones, J. W. (2008) Microstructural influences on very-high-cycle fatigue-crack initiation in Ti-6246. *Metall. Mater. Trans. A*, **39**, 2841–2851.
12 Bache, M. (1997) Dwell sensitive fatigue in a near alpha titanium alloy at ambient temperature. *Int. J. Fatigue*, **19**, 83–88.
13 Pilchak, A. L. and Williams, J. C. (2011) Observations of facet formation in near-α titanium and comments on the role of hydrogen. *Metall. Mater. Trans. A*, **42**, 1000–1027.
14 Venkatramani, G., Ghosh, S. and Mills, M. (2007) A size-dependent crystal plasticity finite-element model for creep and load shedding in polycrystalline titanium alloys. *Acta Mater.*, **55**, 3971–3986.
15 Venkataramani, G., Kirane, K. and Ghosh, S. (2008) Microstructural parameters affecting creep induced load shedding in Ti-6242 by a size dependent crystal plasticity FE model. *Int. J. Plast.*, **24**, 428–454.
16 Dunne, F. P. E., Walker, A. and Rugg, D. (2007) A systematic study of hcp crystal orientation and morphology effects in polycrystal deformation and fatigue. *Proc. R. Soc. A Math. Phys. Eng. Sci.*, **463**, 1467–1489.
17 Zhang, Z., Cuddihy, M. A. and Dunne, F. P. E. (2015) On rate-dependent polycrystal deformation: the temperature sensitivity of cold dwell fatigue. *Proc. R. Soc. A Math. Phys. Eng. Sci.*, **471**, 20150214.
18 Anahid, M., Chakraborty, P., Joseph, D. S. and Ghosh, S. (2009) Wavelet decomposed dual-time scale crystal plasticity FE model for analyzing cyclic deformation induced crack nucleation in polycrystals. *Model. Simul. Mater. Sci. Eng.*, **17**, 064009.
19 Anahid, M., Samal, M. K. and Ghosh, S. (2011) Dwell fatigue crack nucleation model based on crystal plasticity finite element simulations of polycrystalline titanium alloys. *J. Mech. Phys. Solids*, **59**, 2157–2176.
20 Ghosh, S. and Anahid, M. (2013) Homogenized constitutive and fatigue nucleation models from crystal plasticity FE simulations of Ti alloys, Part 1: macroscopic anisotropic yield function. *Int. J. Plast.*, **47**, 182–201.
21 Anahid, M. and Ghosh, S. (2013) Homogenized constitutive and fatigue nucleation models from crystal plasticity FE simulations

of Ti alloys, Part 2: macroscopic probabilistic crack nucleation model. *Int. J. Plast.*, **48**, 111–124.
22 Groeber, M. A. and Jackson, M. A. (2014) DREAM.3D: a digital representation environment for the analysis of microstructure in 3D. *Integr. Mater. Manuf. Innov*, **3**, 5.
23 Groeber, M., Ghosh, S., Uchic, M. D. and Dimiduk, D. M. (2008) A framework for automated analysis and simulation of 3D polycrystalline microstructures. Part 1: statistical characterization. *Acta Mater.*, **56**, 1257–1273.
24 Groeber, M., Ghosh, S., Uchic, M. D. and Dimiduk, D. M. (2008) A framework for automated analysis and simulation of 3D polycrystalline microstructures. Part 2: synthetic structure generation. *Acta Mater.*, **56**, 1274–1287.
25 SIMMETRIX Inc. at <http://www.simmetrix.com/>
26 Neeraj, T. and Mills, M. (2001) Short-range order (SRO) and its effect on the primary creep behavior of a Ti–6wt.%Al alloy. *Mater. Sci. Eng. A*, **319–321**, 415–419.
27 Chichili, D. R., Ramesh, K. T. and Hemker, K. J. (1998) The high-strain-rate response of alpha-titanium: experiments, deformation mechanisms and modeling. *Acta Mater.*, **46**, 1025–1043.
28 Paton, N. E., Baggerly, R. G. and Williams, J. C. (1976) Deformation and solid solution strengthening of titanium-aluminum single crystals. Report SC526. 7FR, Rockwell International Science Center.
29 Williams, J. C., Baggerly, R. G. and Paton, N. E. (2002) Deformation behavior of HCPTi-Al alloy single crystals. *Metall. Mater. Trans. a-Physical Metall. Mater. Sci.*, **33**, 837–850.
30 Venkataramani, G., Deka, D. and Ghosh, S. (2006) Crystal plasticity based Fe model for understanding microstructural effects on creep and dwell fatigue in Ti-6242. *J. Eng. Mater. Technol.*, **128**, 356–365.
31 Lee, B., Vecchio, K., Ahzi, S. and Schoenfeld, S. (1997) Modeling the mechanical behavior of tantalum. *Metall. Mater. Trans. A.*, **28**, 113–122.
32 Asaro, R. J. and Rice, J. R. (1977) Strain localization in ductile single crystals. *J. Mech. Phys. Solids*, **25**, 309–338.
33 Keshavarz, S. and Ghosh, S. (2015) Hierarchical crystal plasticity FE model for nickel-based superalloys: sub-grain microstructures to polycrystalline aggregates. *Int. J. Solids Struct.*, **55**, 17–31.
34 Arsenlis, A. and Parks, D. (1999) Crystallographic aspects of geometrically-necessary and statistically-stored dislocation density. *Acta Mater.*, **47**, 1597–1611.
35 Ogi, H., Kai, S., Ledbetter, H., Tarumi, R., Hirao, M. and Takashima, K. (2004) Titanium's high-temperature elastic constants through the hcp–bcc phase transformation. *Acta Mater.*, **52**, 2075–2080.
36 Heckel, T. K., Guerrero-Tovar, A. and Christ, H.-J. (2011) Stress-dependent elastic behaviour of a titanium alloy at elevated temperatures. *Exp. Mech.*, **52**, 323–329.
37 Dohrmann, C. R., Heinstein, M. W., Jung, J., Key, S. W. and Witkowski, W. R. (2000) Node-based uniform strain elements for three-node triangular and four-node tetrahedral meshes. *Int. J. Numer. Methods Eng.*, **47**, 1549–1568.
38 Puso, M. A. and Solberg, J. (2006) A stabilized nodally integrated tetrahedral. *Int. J. Numer. Methods Eng.*, **67**, 841–867.
39 Cheng, J., Shahba, A. and Ghosh, S. (2016) Stabilized tetrahedral elements for crystal plasticity finite element analysis overcoming volumetric locking. *Comput Mech.* doi:10.1007/s00466-016-1258-2.
40 Neto, E. A. d. S., Pires, F. M. A. and Owen, D. R. J. (2005) F-bar-based linear triangles and tetrahedra for finite strain analysis of nearly incompressible solids. Part I: formulation and benchmarking. *Int. J. Numer. Methods Eng.*, **62**, 353–383.
41 Li, H., Mason, D. E., Bieler, T. R., Boehlert, C. J. and Crimp, M. A. (2013) Methodology for estimating the critical resolved shear stress ratios of α-phase Ti using EBSD-based trace analysis. *Acta Mater.*, **61**, 7555–7567.
42 Stroh, A. N. (1954) The formation of cracks as a result of plastic flow. *Proc. R. Soc. A Math. Phys. Eng. Sci.*, **223**, 404–414.
43 Bažant, Z. P. and Pijaudier-Cabot, G. (1988) Nonlocal continuum damage, localization instability and convergence. *J. Appl. Mech.*, **55**, 287.
44 Sinha, V., Mills, M. J. and Williams, J. C. (2004) Understanding the contributions of normal-fatigue and static loading to the dwell fatigue in a near-alpha titanium alloy. *Metall. Mater. Trans. A*, **35**, 3141–3148.
45 Lütjering, G. and Williams, J. C. (2007) *Titanium*. Springer, Berlin Heidelberg. doi:10.1007/978-3-540-73036-1
46 Nie, Y. and Xie, Y. (2007) Ab initio thermodynamics of the hcp metals Mg, Ti, and Zr. *Phys. Rev. B*, **75**, 174117.
47 Souvatzis, P., Eriksson, O. and Katsnelson, M. I. (2007) Anomalous thermal expansion in α-titanium. *Phys. Rev. Lett.*, **99**, 015901.
48 Nyakana, S. L., Fanning, J. C. and Boyer, R. R. (2005) Quick reference guide for β titanium alloys in the 00s. *J. Mater. Eng. Perform.*, **14**, 799–811.
49 Szczepanski, C. J., Jha, S. K., Larsen, J. M. and Jones, J. W. (2012) The role of local microstructure on small fatigue crack propagation in an α + β titanium alloy, Ti-6Al-2Sn-4Zr-6Mo. *Metall. Mater. Trans. A*, **43**, 4097–4112.
50 Geathers, J., Torbet, C. J., Jones, J. W. and Daly, S. (2015) Investigating environmental effects on small fatigue crack growth in Ti–6242S using combined ultrasonic fatigue and scanning electron microscopy. *Int. J. Fatigue*, **70**, 154–162.
51 Knobbe, H., Köster, P., Christ, H.-J., Fritzen, C.-P. and Riedler, M. (2010) Initiation and propagation of short fatigue cracks in forged Ti6Al4V. *Procedia Eng.*, **2**, 931–940.
52 Hoffmann, C., Eylon, D. and McEvily, A. J. (1982) Influence of microstructure on elevated-temperature fatigue resistance of a titanium alloy. *Low-cycle fatigue and life prediction*, 5–22. doi:10.1520/STP32420S.